Electrochimica Acta 203 (2016) 171–177

Contents lists available at ScienceDirect

Electrochimica Acta

journal homepage: www.elsevier.com/locate/electacta

Stationary Full Li-Ion Batteries with Interlayer-Expanded V_6O_{13} Cathodes and Lithiated Graphite Anodes

Na Xu, Xiaoxuan Ma, Mengfan Wang, Tao Qian*, Jiaqi Liang, Wanli Yang, Ying Wang, Jun Hu*, Chenglin Yan*

College of Physics, Optoelectronics and Energy & Collaborative Innovation Center of Suzhou Nano Science and Technology, Soochow University, Suzhou 215006, China

ARTICLE INFO

Article history:
Received 7 March 2016
Received in revised form 7 April 2016
Accepted 9 April 2016
Available online 11 April 2016

Keywords:
Full batteries
Ultra-stable cathodes
V_6O_{13}
Interlayer expanded
Ultrathin nanosheets

ABSTRACT

Here we report a Li-metal-free full battery, using interlayer-expanded V_6O_{13} ultra-thin nanosheets and prelithiated graphite for cathodes and anodes, respectively. This full Li-ion battery exhibits a superior specific capacity of 233 mAh g^{-1} at a current density of 100 mA g^{-1} and 91% capacity retention after 500 cycles. Our first-principle calculations reveal that the interlayer-expansion is induced by the interaction between V_6O_{13} and water which breaks interlayer V-O bonds and forms hydroxyls. The unique structure provides short lithium-ion diffusion path, excellent charge transport, abundant binding sites and volume flexibility for Li^+ intercalation/deintercalation, thus leading to high capability (280 mAh g^{-1}) and cycling performance (capacity retain 96.1% at 2.4 A g^{-1} for 1000 cycles). Using novel prelithiation process, the Li-metal-free full cells with high controllability and performance is expected to contribute significantly to the development of safe, green, and powerful energy storage devices.

1. Introduction

The sustainable and clean energy sources, derived from solar energy, hydropower, tidal energy, and geothermal heat, have been increasingly demanded due to the pollution of traditional non-renewable fossil resources. With the development of the renewable energy, it is now essential that energy storage devices are required to design to satisfy the power needs of storing a fair amount of energy. Lithium-ion batteries (LIBs) which coupled with high capacity, working voltage, and low toxicity are considered as one of the most promising energy storage devices [1–6]. However, commercialization of full LIBs has so far been limited due to both the energy density and power density problems associated with the tradition cathode materials such as $LiMn_2O_4$ and $LiCoO_2$.

Vanadium oxides have been widely investigated due to their low cost, easy to synthesize, being relatively environmentally friendly and high theoretical capacity (294 mAh g^{-1} with 2 Li^+ ions inserted/extracted per unit formula) [7,8]. Amongst various vanadium oxides (e.g., V_2O_5 [9], VO_2 [10], V_2O_3 [11], V_3O_7 [12], V_6O_{13} [13], etc.), V_6O_{13} exists an impressive capacity, and energy density, due to the large number of lithium ions that can be reversibly intercalated into the V lattice [14]. Theoretically, V_6O_{13} can electrochemically incorporate up to 8 Li^+ per formula unit with all the V ions being reduced to 3+ oxidation state, which gives a high theoretical specific capacity and energy of 417 mAh g^{-1} and 900 Wh kg^{-1} [15], respectively, much higher than those of conventional $LiMn_2O_4$ (148 mAh g^{-1}, 500 Wh kg^{-1}) [16], $LiCoO_2$ (140 mAh g^{-1}, 540 Wh kg^{-1}) [17]. However, it is difficult to achieve high capacities with good cyclability for V_6O_{13} cells because of the phase transitions, which decrease in electronic conductivity upon lithium insertion, and the loss of electrode integrity [18]. Moreover, Li^+ ions exist as interstitial impurities in perfectly crystallized V_6O_{13} and interact strong with the lattice O anions, which results in considerably slow mobility of Li^+ ions. In order to overcome these prejudicious issues, two approaches may be used: (1) introducing dipole molecules (e.g., H_2O) in the host lattice to transform Li^+ into much less polarizing solvated ions, thereby alleviating the host-guest interaction and increasing the ion diffusivity [19]; (2) drastically down-sizing the particles to nanoscale so that the Li diffusion length is short enough to ensure a decent apparent Li diffusivity [20,21].

Another major concern regarding LIBs system is the use of lithium-metal anode, which is well known to have some critical defects including chemical reactivity in commonly used organic electrolytes and dendritic growth of lithium during cycling, thus

* Corresponding authors.
E-mail addresses: tqian@suda.edu.cn (T. Qian), jhu@suda.edu.cn (J. Hu), c.yan@suda.edu.cn, chenglinyan.nano@gmail.com (C. Yan).

http://dx.doi.org/10.1016/j.electacta.2016.04.044
0013-4686/

leading to poor cycle and safety performance. Recently, carbon-type anode materials have been suggested as alternatives to replace the lithium-metal anode. Nevertheless, carbon-type anodes can only couple with lithium metal oxide cathodes such as $LiCoO_2$ [22], $LiNiO_2$ [23], $LiMn_2O_4$ [24], $LiFePO_4$ [25] to construct full batteries and deliver high power, thus making it a major challenge to effectively combine carbon-type anodes with Li-metal-free cathodes to form a full cell.

Herein, we demonstrate a stationary full cell configuration with a novel interlayer-expanded $V_6O_{13}{\cdot}nH_2O$ ultra-thin nanosheets (IEVOS) cathode and lithiated graphite anode. Our IEVOS introduce interlayer expansion as a general and effective approach to increase the intrinsic Li diffusivity of layer-structured intercalation hosts by modifying the lattice structure meanwhile weakening the interaction between Li^+ and the host without introducing adverse side effects. Inclusion of dipole molecules such as hydroxy radical in the lattice converts Li^+ to less polarizing solvated cations, thus foster electron transfer and intercalation of highly charged Li^+ ions. A peculiar technique was used to handle the commercial graphite which can provide the anode material ample source of Li^+. As a result of the above benefits, the assembled full battery delivers an improved capacity (233 mAh g^{-1} with an average working voltage of about 2.4 V), high energy density (116.5 Wh kg^{-1} based on the weight of active materials on the cathode and anode) and excellent cycling stability (nearly 91% capacity retention after 500 cycles at current density of 900 mA g^{-1}), which are much better than those of previous reported full cells. These results could advance the development of practical LIBs to a large extent, particularly for use in zero-emission vehicles. Safer, greener, and more powerful LIBs can be achieved by the new Li-metal-free process.

2. Results and discussion

The structures of the IEVOS samples were first examined by field emission scanning electron microscopy (FESEM) and High resolution transmission electron microscopy (HRTEM) measurements. As revealed by Fig. S1A and Fig. S1B, hollow microspheres with uniform size were obtained after hydrothermal reaction for 3 h. The FESEM image of the product (Fig. 1A) exhibits uniform two-dimensional (2D) ultra-thin nanosheets morphology with lateral dimensions of *ca.* 8 nm. More fine details are presented by the HRTEM image (Fig. 1B), which shows well-defined lattice fringes of the nanosheets crystals, where the lattice spacing of 1.31 nm is consistent with the (001) crystalline plane of IEVOS. Furthermore, a uniform thin carbon layer of *ca.*1.5 nm covers the surface of the nanosheets, which is also proved by the HRTEM image.

The crystal structures of IEVOS and stacked V_6O_{13} (SVO) were determined by X-ray diffraction (XRD) (Fig. 1C). The XRD patterns of the samples are both well indexed to monoclinic V_6O_{13} (lattice parameters a = 11.96 Å, b = 3.713 Å, c = 10.07 Å, β = 100.9°, JCPDS no.: 71–0297) and the interlayer distance is studied with the patterns. The lattice parameters were calculated from the XRD patterns as an average of six maximum intensity peaks of the IEVOS (001, 110, 003, 412, 020, and 62-1 planes) using MDI Jade 5.0 software. The lattice parameters were calculated for a = 13.455 Å, b = 3.728 Å, c = 14.188 Å, β = 100.48° with the space-group C2/m, which illustrate the swell in both a-direction and c-direction of the crystal structure. The diffraction peak appear at lower angles which indicates a bigger lattice distance according to Bragg's formula ($d = 0.5\,\lambda/\sin(\theta)$). The crystal structure is separated by large interlayer spacing corresponds to a diffraction peak at $2\theta = 6.9°$ and the interlayer distance is calculated to be 1.31 nm, which is according with the result of HRTEM image. For the pattern of IEVOS, the intensity of the diffraction peak much bigger than that of SVO, illustrating more interlayers are expanded with the ultra-thin nanosheets structures. Moreover, the XRD pattern of IEVOS are studied after a dehydration process (annealed at 800 °C under N_2 gas flow), which noted as DHVOS (Fig. S2). It is obviously that the peak attributed to the lattice distance of 1.31 nm is devided

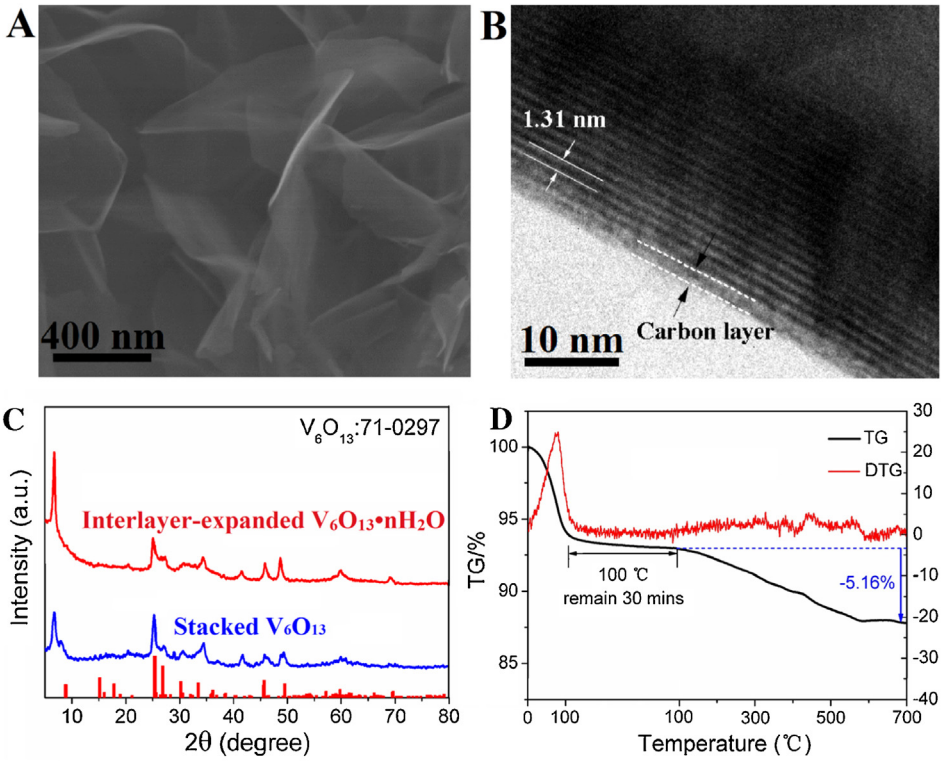

Fig. 1. (A) FESEM and (B) HRTEM images of IEVOS. (C) XRD patterns of as-prepared IEVOS and SVO. (D) TG and DTG curves of IEVOS in N_2.

into three weaker peaks centre at 2θ = 8.5°, 10.1°, 12.2°, implying the decreased lattice spaces. The phenomena reveal that the existence of crystal water is the primary cause of the interlayer expanding of IEVOS.

To accurately determinate the amount of crystal water, thermogravimetry (TG) and dynamic thermogravimetry (DTG) of IEVOS were measured. It can be seen clearly in Fig. 1D, the weight change profile for the oxide is characterized by a steep loss between room temperature and 100 °C, followed by a more gradual weight loss up until 580 °C. With the first steep loss, DTG curve has an obvious peak meaning a endothermic reaction is happened during this section, which attribute to the loss of absorbed water during 0 to 100 °C. When it comes to the second largo loss, the weight loss starts at 100 °C and continues to 580 °C with an inconspicuous endothermic process is due to the loss of crystal water in IEVOS. And based on the above TG and DTG tests, it is also can be calculated that, the existence of 1.67 mol of crystal water per mole of oxide at room temperature.

To reveal the atomic structure of IEVOS, we carried out first-principle calculations. The crystal structure of V_6O_{13} consists of quasi two-dimensional single and double trellis layers parallel to *a-b* plane, as marked by 'A' and 'B' in Fig. 2. Both layers are composed of VO_6 octahedra and share the O atoms between them as marked by 'C'. The V ions are in a mixed valence states V^{5+} and V^{4+} with a ratio of 1:2. Our calculations reveal that the local magnetic moments on V^{4+} ions exhibit antiferromagnetic long-range ordering, in good agreement with previous studies [26,27]. To reveal the form of water in V_6O_{13}, we considered several different configurations and compared their total energies. The most stable configuration indicates that the strong interaction between water molecules and the lattice O ions in the 'C' layer breaks the V-O-V bonds and the water molecules, forming hydroxyl radicals on both sides. Consequently, new layered structure forms with inter-layer spacing of ~3.4 Å and the layers couple with each other through Van der Waals force. The optimized lattice constants are close to our experimental measurement. Obviously, the significant expansion of the lattice gives rise to much more free space for Li ions to diffuse compared with the original V_6O_{13}. In fact, the binding energy between Li ions and V_6O_{13}, $E_b = E(V_6O_{13} + Li) - E(V_6O_{13}) - E(Li)$, is as large as −3.4 eV, indicating strong interaction between Li and lattice O ions. On the contrary, E_b of Li in IEVOS reduces to −1.9 eV, resulting in remarkable enhancement of the mobility of Li ions. Clearly, our theoretical modeling not only reveals the atomic structure of IEVOS, but also gives the underlying mechanism of the significant enhancement of the Li capacity and cycling stability.

The electrochemical performance of the full cell configuration with IEVOS cathode and lithiated graphite anode is shown in Fig. 3. The representative charge/discharge curves of the 1st, 4th and 5th cycles at a current density of 100 mA g^{-1} (Fig. 3A) delivers a capacity of *ca.* 233 mAh g^{-1} (respect to the mass of IEVOS), which resulted in a high specific energy of 116.5 Wh kg^{-1} (respect to the overall mass of IEVOS cathode and lithiated graphite anode). The discharge capacity falls to 228 mAh g^{-1} at the 4th cycle and remained at 5th cycle, at which point the discharge capacity tends to stabilize. Further, the rate capability of full battery was characterized through subjecting to high current rates to evaluate the rate capability with various applied current densities. It is obvious to notice from Fig. 3B that even at the ultra-high rate of 900 mA g^{-1}, the full cell was able to deliver substantial capacity of 140 mAh g^{-1}, which indicating the excellent rate capability of both materials and resulted in a high power density of 450 W kg^{-1}. Ragone plots of the full cell describing the relationship between energy density and power density were obtained and shown in Fig. S4, the specific energy still maintained 140 mAh g^{-1} when the specific power was increased to 450 W kg^{-1}, which illustrates that the energy density and power density of the prepared full cells are considerably higher than those of previous works. It should be noted that the full cell maintained about 91% of its initial specific capacity over 500 cycles at a current density of 900 mA g^{-1} (Fig. 3C), implying that the cycle life of the full cell reported herein reaches and even more outstanding than that of commercial lithium-ion batteries and other publications (Table S1) [28–32].

For gaining insight or an insight into the excellent performance of the presented full cell, the electrochemical properties of the newly designed cathode materials, i.e., ultra-thin $V_6O_{13}{\cdot}nH_2O$ nanosheets with large interlayer spacing had been further investigated. The cathode materials were assembled with lithium metal into coin cells to evaluate their structural advantages in lithium ion insertion/extraction. Cyclic voltammetry (CV) test was first studied within the voltage range of 2–4 V vs. Li/Li^+. As Fig. 4A shows, the first ten consecutive CV curves are almost identical and no obvious decay, which suggests the remarkable reversibility of the electrode upon cycling. One pair of well-defined anodic and cathodic peaks assigned at 2.39 and 2.76 could be also noticed, and the narrow potential gaps between the peaks demonstrate the low polarization between the electrode and electrolyte [33].

The individual 1st, 2nd, 5th, 10th and 20th cycle charge/discharge curves of IEVOS at a low current density of 100 mA g^{-1} are shown in Fig. 4B, which delivers a discharge capacity of 280 mAh g^{-1}. Good reversible plateau regions can be observed and

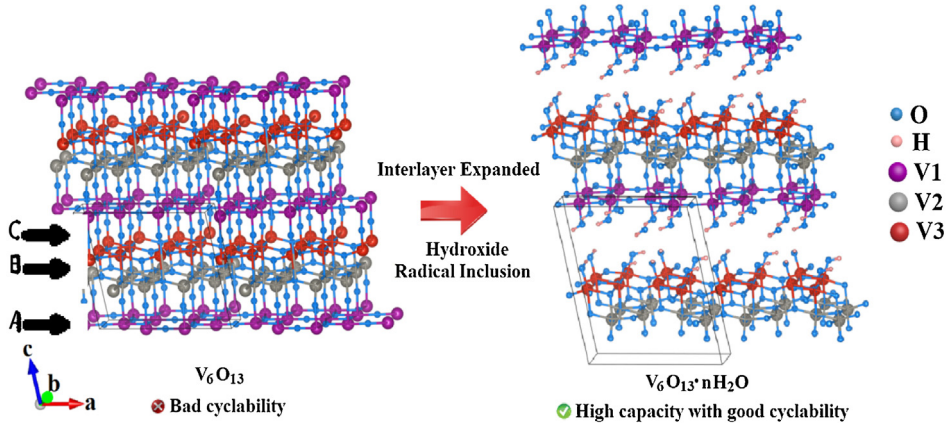

Fig. 2. Theoretical consideration of the refined structure of V_6O_{13} and interlayer expanded $V_6O_{13}{\cdot}nH_2O$ by the first-principle calculation.

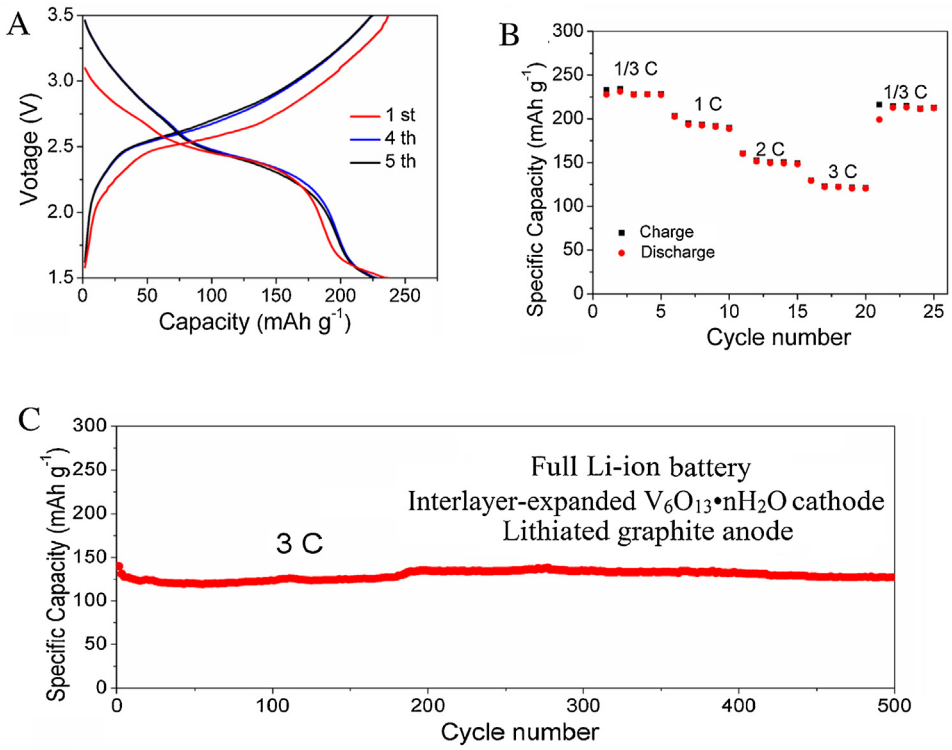

Fig. 3. (A) Voltage profiles plotted of full cell for the first, fourth and fifth cycles at a current density of 100 mA g^{-1}. (B) The rate capability of IEVOS/lithiated graphite from 1/3C to 3C (1 C = 300 mA g^{-1}). (C) Cycling performance of the prepared full cell.

the discharge/charge plateaus agree well with the peaks shown in the CV curves. The discharge and charge curves are generally remain stable over the repeated cycles, which indicate the good structural reversibility of the cathode materials.

Besides the obtained high capacity, IEVOS electrodes demonstrate satisfactory rate capability as well (Fig. 4C). At the high rate of 2400 mA g^{-1}, the delivered capacity is still as high as 153 mAh g^{-1}, and even at the ultrahigh rate of 4800 mA g^{-1}, the cell is able to deliver substantial capacity of 121 mAh g^{-1}, which indicating the excellent rate capability of the material. It should be noted that, after the continuous cycling with increasing current densities, a specific capacity as high as 277 mAh g^{-1} could be well recovered at a current density of 100 mA g^{-1}, that is, about 99% retention of the specific capacity in the second cycle, confirming the excellent Li^+ storage reversibility.

As for cycling tests in Fig. 4D, as expected, the obtained electrodes also exhibit superior cycling stability which maintained reversible capacity of 191 mAh g^{-1} after 150 cycles at 600 mA g^{-1} corresponding to 93.7% capacity retention compared with the first discharge capacity, with a high coulombic efficiency of >99% throughout. Fig. 4E shows the cycling behavior of IEVOS and DHVOS electrodes at the current densities of 2400 mA g^{-1}. The maximum specific discharge capacities of IEVOS is 142 mA h g^{-1} which is ascribed to the existence of hydroxyl [34] and is much higher than that of DHVOS (60 mA h g^{-1}). It is astounding that IEVOS retain 96.1% of the initial capacity with an average capacity fading rate of 0.0039% per cycle; nevertheless, SVO can only retain 46.4% (Fig. S5) after 1000 cycles, since most of SVO lattice spacing were not expanded by hydroxyl (Fig. 1C).

In order to further confirms the Li+ ion diffusion coefficients of IEVOS and DHVOS, CV tests of the half batteries at various scan rates are displayed in Fig. 5, from which the increased cathode-anode peak differences with the increasing of scan rates indicate an enlarged irreversibility at high current densities. As can be seen from Fig. 5C, the peak current density of the intensive anodic reaction i_p is proportional to the square root of the sweep rate $v^{1/2}$, which shows the linear semi-infinite diffusion in cathodic and anodic processes. Consequently, the Randles–Sevcik equation (eqn (1)) can be applied [35], based on which the Li^+ ion diffusion coefficient D_{Li+} can be calculated.

$$i_p/m = 0.4463n^{1.5}F^{1.5}CSR^{-0.5}T^{-0.5}D^{0.5}v^{0.5} \quad (1)$$

where *m* is the mass of active cathode material (g), *n* is the number of electrons in reaction, *F* is the Faraday constant (96485C mol^{-1}), *R* is the gas constant (8.314 J mol^{-1} K^{-1}), *T* is the absolute temperature (K), S is the surface area per unit weight of active materials (10^{-3} g cm^{-2}), D is the diffusion constant (cm^2 s^{-1}), *v* is the scan rate of the CV test (V s^{-1}) and the lithium ion concentration C is 0.001 mol cm^{-3}. Herein, the IEVOS and DHVOS could produce cathodic D_{Li+} value of 5.447×10^{-7} cm^2 s^{-1} and 0.9899×10^{-7} cm^2 s^{-1}, respectively, and it's clear that the Li^+ value of DHVOS is much lower than that of IEVOS which should be attributed to the ultra-large interlayer distance for litium ions in transportation. It can also prove that the existence of a predominately lithium-ion diffusion in large interlayer distance for lithium battery, results in high D value, otherwise, the value might be lower as a result of the effects from Li ions.

The EIS is monitored during 1st to 500th cycles to gain further insight into the electrode changes upon lithium ion insertion/extraction cycles (Fig. 5D). The inset shows an equivalent circuit model according to the simulation, in which R_s represents the equivalent series resistance that includes all ohmic resistance due to the electrolyte and other parts of the cell. R_{ct} stand for the charge transfer resistance through the electrode/electrolyte interface, while CPE refer to double-layer capacitance. Z_W represents Warburg impedance, which is described as a diffusive resistance

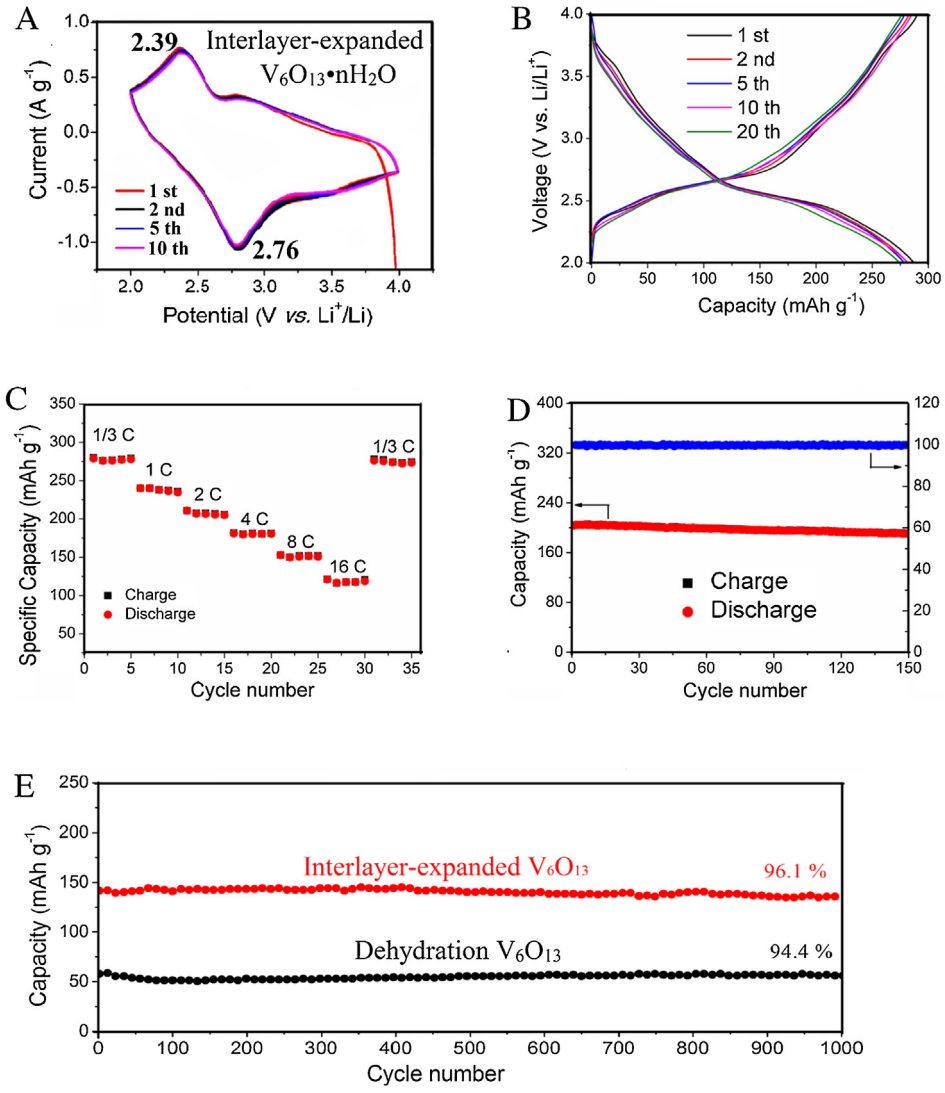

Fig. 4. (A) Representative CV curves of an electrode based on the IEVOS obtained at a voltage range of 2 to 4 V (vs. Li^+/Li) and potential scan rate of 0.05 mV s^{-1}. (B) Voltage profiles plotted for the first, second, fifth, tenth, twentieth cycles at a current density of 100 mA g^{-1}. (C) The rate capability from 1/3C–16C (1 C = 300 mA g^{-1}). (D) Cycling performance at current densities of 600 mA g^{-1} at a voltage range of 2 to 4 V. (E) Cycling performance of IEVOS and DHVOS at current densities of 2.4 A g^{-1} at a voltage range of 2 to 4 V.

of the Li^+ within the electrode pores [36]. R_{ct} values decrease steeply in the first 50 cycles and then increase slightly in the following cycles. We propose that electrolyte gradually penetrated on the surface of nanosheets and diffuse into the predominantly exposed facets after the first few cycles which should facilitate the electro chemical reaction and lead to the decrease of R_{ct}. It is well-known that the slower increase of resistance during cycles means lower polarization. Hence, the subsequent mild R_{ct} increase perfectly illustrates the good cycling behavior of the electrode.

3. Conclusions

In summary, we demonstrated, for the first time, an effective approach to break interlayer V-O bonds and forms hydroxyls which gives rise to expanding the distance between the layers. When applied as cathode materials in LIBs, the IEVOS developed with an excellent capacity of 280 mA g^{-1}, good cyclability (retain 96.1% at 2.4 A g^{-1} for 1000 cycles) as well as rate capability (121 mAh g^{-1} at 4.8 A g^{-1}) arising from the synergetic effect from interlayer-expanded structure and water dipole molecules. With this novel IEVOS cathode materials and lithiated graphite anode materials, an ultra-stable full battery was assembled and delivers a high power density of 450 W kg^{-1} and 91% capacity retention after 500 cycles when cycled at a 3C rate. The Li-metal-free full cell with high controllability and performance is promising to opens up an opportunity to consider these techniques for advancing safe, green, and powerful energy storage.

4. Experimental Section

4.1. Synthesis of IEVOS, SVO and V_6O_{13}

0.045 M V_2O_5 and 0.135 M $H_2C_2O_4$ solution was mixed at 90 °C until a dark blue solution was formed. 2.5 mL of the above solution was transferred into a teflon-lined stainless steel autoclave. Then 0.5 mL of H_2O_2 and 10 mL ethanol was added and kept at 180 °C for 3 h. Finally, the samples were dried at 60 °C in vacuum for 12 h. IEVOS were annealed at 800 °C under N_2 gas flow to fabricate V_6O_{13}. SVO was obtained through a similar method to that of IEVOS with double concentration of V_2O_5 and $H_2C_2O_4$.

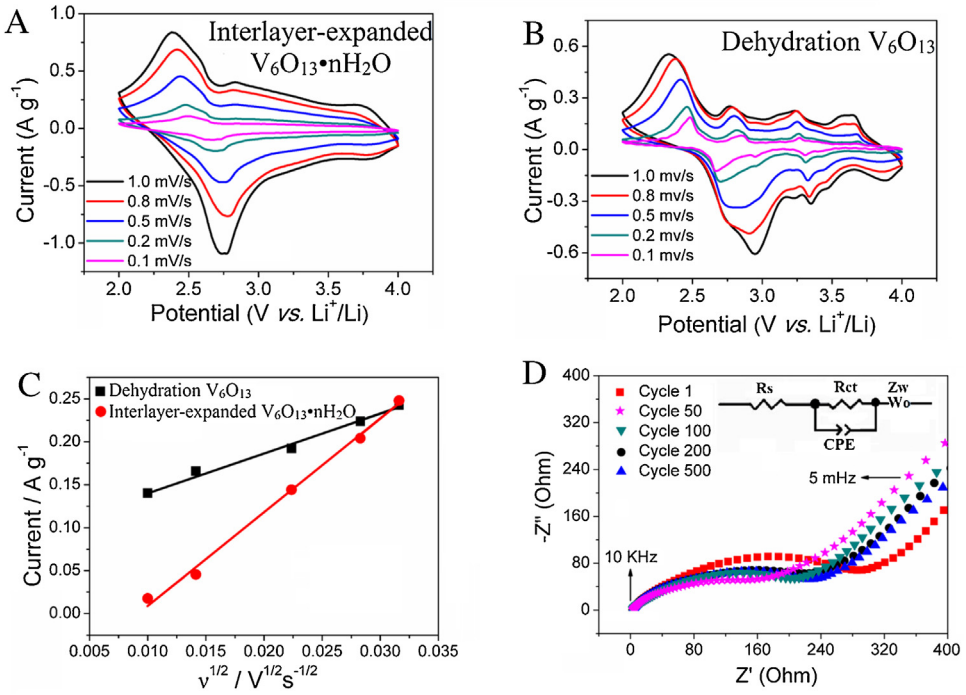

Fig. 5. CV curves at different scan rates of (A) IEVOS and (B) DHVOS. (C) The corresponding relationship between the square root of the scan rate $v^{1/2}$ and peak current i_p of IEVOS and DHVOS in a voltage range of 2–4 V vs. Li^+/Li. (D) AC impedance plots at full charged state after different cycles.

4.2. Structure Characterization

The morphology was investigated by field emission scanning electron microscopy (FESEM, SU8010, Japan), and field emission transmission electron microscopy (FETEM, FEI Tecnai G2 F20 S-TWIN TMP, Hongkong). Surface elemental analysis was performed on an X-ray photoelectron spectrometer (XPS, Kratos Axis Ultra Dld, Japan). X-ray diffraction (XRD) measurements were taken on a Rigaku D/max-2000PC diffractometer with Cu KR radiation in a 2θ range from 5° to 80° at room temperature. Thermogravimetric (TG) was measured by a TG-DTA thermogravimetric analyzer (SII NanoTechnology Inc, Japan).

4.3. Electrochemical Characterization

The cathode slurry was prepared by dispersing IEVOS, acetylene black and polytetrauoroethylene (PTFE; 60 wt % dispersion in water) in ethanol with a weight ratio of 7:2:1. The slurry was spread on titanium foil disks and dried in a vacuum oven at 60 °C overnight prior to coin cells assembly (loading density of 1.0-1.5 mg cm^{-2}). For the half cell, lithium foil was used as the counter and reference electrode, and 1.0 M $LiPF_6$ in ethylene carbonate/ethyl methyl carbonate/dimethyl carbonate (4:3:3 vol. %) was used as the electrolyte. The assembly of the cell was conducted in an Ar-filled glovebox followed by a six hours aging treatment before the test. Cyclic voltammetry (CV) measurement was conducted on a CHI 660E (Chenhua Shanghai, China) electrochemical workstation. Electrochemical impedance spectroscopy (EIS) was also performed on this electrochemical workstation over the frequency range from 10 kHz to 0.005 Hz. The cycle life and rate capability of the cells were tested within a voltage window of 2–4 V (*vs.* Li^+/Li) by using a battery testing system (LAND CT 2001A, Wuhan, China) at room temperature. Prior to use in full cell, the graphite-based anode was pre-lithiated for several hours by directly pressing it against lithium metal wetted by the $LiPF_6$ electrolyte. The full cells were assembled by coupling in a LIR2025 coin-type cell and galvanostatic tests were carried out within a voltage window of 1.5-3.5 V. The graphite loading was about 1.5 mg cm^{-2} and the IEVOS loading was about 1 mg cm^{-2}. The energy density (E) of the samples was calculated using the formula, E = 1/4CV, where C is the capacity (mAh g^{-1}) and V is the average working potential (V) of the electrode. The corresponding power density (P) of the samples was calculated using the formula, P = E/Δt, where E is the energy density and Δt (h) is the discharge time.

4.4. Details of Theoretical Calculations

Spin-polarized density functional calculations were carried out with the Vienna *ab initio* simulation package (VASP) [37,38], at the level of the generalized gradient approximation (GGA) using the PW91 functional [39]. We took into account the Hubbard-type repulsive interation (GGA + *U*) to improve the description of electron correlations in the V-3d orbitals [40]. Here we chose U = 5 eV which reproduces experimental band gap in the insulating phase [41]. We used the projector augmented wave (PAW) method for the description of the core-valence interaction [42,43]. The energy cutoff for the basis expansion was set to 600 eV. The Brillouin zone was sampled by a $3 \times 9 \times 3$ k-grid mesh [44]. All atoms were fully relaxed until the calculated force on each atom was smaller than 0.01 eV/Å.

Acknowledgements

We acknowledge the support from the "Thousand Talents Program", the Natural Science Foundation of Jiangsu Province of China (no. BK20140315, no. BK20150338), the National Natural Science Foundation of China (no. 51402202), the National Basic Research Program of China (no. 2015CB358600), the Jiangsu Shuangchuang Plan, the Priority Academic Program Development of Jiangsu Higher Education Institutions (PAPD), and China Postdoctoral Science Foundation Funded Project (no. 2015M570474).

Appendix A. Supplementary data

Supplementary data associated with this article can be found, in the online version, at http://dx.doi.org/10.1016/j.electacta.2016.04.044.

References

[1] G. Gershinsky, E. Bar, L. Monconduit, D. Zitoun, Operando electron magnetic measurements of Li-ion batteries, Energy Environ. Sci. 7 (2014) 2012.
[2] S. Tepavcevic, H. Xiong, V.R. Stamenkovic, X.B. Zuo, M. Balasubramanian, V.B. Prakapenka, C.S. Johnson, T. Rajh, Nanostructured Bilayered Vanadium Oxide Electrodes for Rechargeable Sodium-Ion Batteries, ACS Nano 6 (2012) 530.
[3] M. Yan, F. Wang, C. Han, X. Ma, X. Xu, Q. An, L. Xu, C. Niu, Y. Zhao, X. Tian, P. Hu, H. Wu, L. Mai, Nanowire Templated Semihollow Bicontinuous Graphene Scrolls: Designed Construction Mechanism, and Enhanced Energy Storage Performance, J. Am. Chem. Soc. 135 (2013) 18176.
[4] J.L. Xie, C.X. Guo, C.M. Li, Construction of one-dimensional nanostructures on graphene for efficient energy conversion and storage, Energy Environ. Sci. 7 (2014) 2559.
[5] B. Kang, G. Ceder, Battery materials for ultrafast charging and discharging, Nature 458 (2009) 190.
[6] M. Armand, J.M. Tarascon, Building better batteries. Nature 451 (2008) 652.
[7] C.F. Zhang, Z.X. Chen, Z.P. Guo, X.W. Lou, Additive-free synthesis of 3D porous V_2O_5 hierarchical microspheres with enhanced lithium storage properties, Energ. Environ. Sci. 6 (2013) 974.
[8] M. Sathiya, A. Prakash, K. Ramesha, J.M. Tarascon, A.K. Shukla, V_2O_5-anchored carbon nanotubes forenhanced electrochemical energy storage, J. Am. Chem. Soc. 133 (2011) 16291.
[9] T. Qian, N. Xu, J.Q. Zhou, T.Z. Yang, X.J. Liu, X.W. Shen, J.Q. Liang, C.L. Yan, Interconnected three-dimensional V_2O_5/polypyrrole network nanostructures for high performance solid-state supercapacitors, J. Mater. Chem. A 3 (2015) 488.
[10] L.Q. Mai, Q.L. Wei, Q.Y. An, X.C. Tian, Y.L. Zhao, X. Xu, L. Xu, L. Chang, Q.J. Zhang, Nanoscroll Buffered Hybrid Nanostructural VO_2 (B) Cathodes for High-Rate and Long-Life Lithium Storage, Adv. Mater. 25 (2013) 2969.
[11] H.Y. Li, K. Jiao, L. Wang, C. Wei, X.L. Li, B. Xie, Micelle anchored in situ synthesis of V_2O_3 nanoflakes@C composites for supercapacitors, J. Mater. Chem. A 2 (2014) 18806.
[12] Y.L. Ding, Y.R. Wen, C. Wu, P.A.V. Aken, J. Maier, Y. Yu, 3D V_6O_{13} Nanotextiles Assembled from Interconnected Nanogrooves as Cathode Materials for High-Energy Lithium Ion Batteries, Nano Lett. 15 (2015) 1388.
[13] M.Y. Yan, F.C. Wang, C.H. Han, X.Y. Ma, X. Xu, Q.Y. An, L. Xu, C.J. Niu, Y.L. Zhao, X. C. Tian, P. Hu, H.G. Wu, L.Q. Mai, Nanowire Templated Semihollow Bicontinuous Graphene Scrolls: Designed Construction Mechanism, and Enhanced Energy Storage Performance, J. Am. Chem. Soc. 135 (2013) 18176.
[14] N.A. Chernova, M. Roppolo, A.C. Dillon, M.S. Whittingham, Layered vanadium and molybdenum oxides: batteries and electrochromics, J. Mater. Chem. 19 (2009) 2526.
[15] H. Li, P. He, Y. Wang, E. Hosono, H. Zhou, High-surface vanadium oxides with large capacities for lithium-ion batteries: from hydrated aerogel to nanocrystalline VO_2 (B), V_6O_{13} and V_2O_5, J. Mater. Chem. 21 (2011) 10999.
[16] A.D. Pasquier, C.C. Huang, T. Spitler, Nano $Li_4Ti_5O_{12}$–$LiMn_2O_4$ batteries with high power capability and improved cycle-life, J. Power Sources 186 (2009) 508.
[17] I.D. Scott, Y.S. Jung, A.S. Cavanagh, Y.F. Yan, A.C. Dillon, S.M. George, S.H. Lee, Ultrathin Coatings on Nano-$LiCoO_2$ for Li-Ion Vehicular Applications, Nano Lett. 11 (2011) 414.
[18] H.L. Fei, Y.S. Lin, M.D. Wei, Facile synthesis of V_6O_{13} micro-flowers for Li-ion and Na-ion battery cathodes with good cycling performance, J. Colloid Interf. Sci. 425 (2014) 1.
[19] F.F. Wu, S.L. Xiong, Y.T. Qian, S.H. Yu, Hydrothermal Synthesis of Unique Hollow Hexagonal Prismatic Pencils of $Co_3V_2O_8{\cdot}nH_2O$: A New Anode Material for Lithium-Ion Batteries, Angew. Chem. Int. Ed. 54 (2015) 10787.
[20] Y. NuLi, J. Yang, Y. Li, J. Wang, Mesoporous magnesium manganese silicate as cathode materials for rechargeable magnesium batteries, Chem. Commun. 46 (2010) 3794.
[21] Y. Liang, R. Feng, S. Yang, H. Ma, J. Liang, J. Chen, Rechargeable Mg Batteries with Graphene-like MoS_2 Cathode and Ultrasmall Mg Nanoparticle Anode, Adv. Mater. 23 (2011) 640.
[22] J.C. Cao, G.R. Hu, Z.D. Peng, K. Du, Y.B. Cao, Polypyrrole-coated $LiCoO_2$ nanocomposite with enhanced electrochemical properties at high voltage for lithium-ion batteries, J. Power Sources 281 (2015) 49.
[23] H.R. Chen, J.A. Dawson, J.H. Harding, Effects of cationic substitution on structural defects in layered cathode materials $LiNiO_2$, J. Mater. Chem. A 2 (2014) 7988.
[24] W. Tang, Y.Y. Hou, F. Wang, L.L. Liu, Y.P. Wu, K. Zhu, $LiMn_2O_4$ Nanotube as Cathode Material of Second-Level Charge Capability for Aqueous Rechargeable Batteries, Nano Lett. 13 (2013) 2036.
[25] Z.Y. Bi, X.D. Zhang, W. He, D.D. Min, W.S. Zhang, Recent advances in $LiFePO_4$ nanoparticles with different morphology for high-performance lithium-ion batteries, RSC Adv. 3 (2013) 19744.
[26] M. Itoh, H. Yasuoka, Y. Ueda, K. Kosuge, NMR study of microscopic magnetic properties of V_6O_{13}, J. Phys. Soc. Jpn. 53 (1984) 1847.
[27] Y. Ueda, K. Kosuge, S. Kachi, Magneto-Torque Measurement on V_6O_{13}, Mater. Res. Bull. 11 (1976) 293.
[28] P. Xiong, L.L. Peng, D.H. Chen, Y. Zhao, X. Wang, G.H. Yu, Two-dimensional nanosheets based Li-ion full batteries with high rate capability and flexibility, Nano Energy 12 (2015) 816.
[29] Y.H. Wang, Y.H. Wang, D.S. Jia, Z. Peng, Y.Y. Xia, G.F. Zheng, All-Nanowire Based Li-Ion Full Cells Using Homologous Mn_2O_3 and $LiMn_2O_4$, Nano Lett. 14 (2014) 1080.
[30] K.S. Eom, T. Joshi, A. Bordes, I. Do, T.F. Fuller, The design of a Li-ion full cell battery using a nano silicon and nano multi-layer graphene composite anode, J. Power Sources 249 (2014) 118.
[31] Y.L. Cheah, V. Aravindan, S. Madhavi, Synthesis and Enhanced Lithium Storage Properties of Electrospun V_2O_5 Nanofibers in Full-Cell Assembly with a Spinel $Li_4Ti_5O_{12}$ Anode, ACS Appl. Mater. Interfaces 5 (2013) 3475.
[32] H.T. Zhou, X.H. Wang, D. Chen, Li-Metal-Free Prelithiation of Si-Based Negative Electrodes for Full Li-Ion Batteries, ChemSusChem 8 (2015) 2737.
[33] S.Q. Liang, Y. Hu, Z.W. Nie, H. Huang, T. Chen, A.Q. Pan, G.Z. Cao, Template-free synthesis of ultra-large V_2O_5 nanosheets with exceptional small thickness for high-performance lithium-ion batteries, Nano Energy 13 (2015) 58.
[34] K. Takahashi, Y. Wang, G.Z. Cao, Ni-$V_2O_5{\cdot}nH_2O$ Core-Shell Nanocable Arrays for Enhanced Electrochemical Intercalation, J. Phys. Chem. B 109 (2005) 48.
[35] H. Kim, J. Lee, H. Ahn, O. Kim, M.J. Park, Synthesis of three-dimensionally interconnected sulfur-rich polymers for cathode materials of high-rate lithium–sulfur batteries, Nat. Commun. 6 (2015) 7278.
[36] Y.F. Dong, S. Li, K.N. Zhao, C.H. Han, W. Chen, B.L. Wang, L. Wang, B.A. Xu, Q.L. Wei, L. Zhang, X. Xu, L.Q. Mai, Hierarchical zigzag $Na_{1.25}V_3O_8$ nanowires with topotactically encoded superior performance for sodium-ion battery cathodes, Energy Environ. Sci. 8 (2015) 1267.
[37] G. Kresse, J. Furthmuller, Efficiency of ab-initio total energy calculations for metals and semiconductors using a plane-wave basis set, Comput. Mater. Sci. 6 (1996) 15.
[38] G. Kresse, J. Furthmuller, Efficient iterative schemes for ab initio total-energy calculations using a plane-wave basis set, Phys. Rev. B 54 (1996) 11169.
[39] J.P. Perdew, J.A. Chevary, S.H. Vosko, K.A. Jackson, M.R. Pederson, D.J. Singh, C. Fiolhais, Atoms, molecules, solids, and surfaces: Applications of the generalized gradient approximation for exchange and correlation, Phys. Rev. B 46 (1992) 6671.
[40] A. Rohrbach, J. Hafner, G. Kresse, Electronic correlation effects in transition-metal sulfides, J. Phys. Condens. Matter 15 (2003) 979.
[41] S. Suga, A. Shigemoto, A. Sekiyama, S. Imada, A. Yamasaki, A. Irizawa, S. Kasai, Y. Saitoh, T. Muro, N. Tomita, K. Nasu, H. Eisaki, Y. Ueda, High-energy angle-resolved photoemission spectroscopy probing bulk correlated electronic states in quasi-one-dimensional V_6O_{13} and $SrCuO_2$, Phys. Rev. B 70 (2004) 155106.
[42] P.E. Blochl, Projector augmented-wave method, Phys. Rev. B 50 (1994) 1758.
[43] G. Kresse, D. Joubert, From ultrasoft pseudopotentials to the projector augmented-wave method, Phys. Rev. B 59 (1999) 1758.
[44] H.J. Monkhorst, J.D. Pack, Special points for Brillouin-zone integrations, Phys. Rev. B 13 (1976) 5188.